

A Comprehensive Study on Visual Explanations for Spatio-temporal Networks

Zhenqiang Li¹, Weimin Wang², Zuoyue Li³, Yifei Huang¹, and Yoichi Sato¹

¹ The University of Tokyo, Japan

² AIST, Tokyo, Japan

³ ETH Zürich, Switzerland

Abstract. Identifying and visualizing regions that are significant for a given deep neural network model, *i.e.*, *attribution methods*, is still a vital but challenging task, especially for spatio-temporal networks that process videos as input. Albeit some methods that have been proposed for video attribution, it is yet to be studied what types of network structures each video attribution method is suitable for. In this paper, we provide a comprehensive study of the existing video attribution methods of two categories, gradient-based and perturbation-based, for visual explanation of neural networks that take videos as the input (spatio-temporal networks). To perform this study, we extended a perturbation-based attribution method from 2D (images) to 3D (videos) and validated its effectiveness by mathematical analysis and experiments. For a more comprehensive analysis of existing video attribution methods, we introduce objective metrics that are complementary to existing subjective ones. Our experimental results indicate that attribution methods tend to show opposite performances on objective and subjective metrics.

1 Introduction

Deep neural networks have achieved remarkable improvements in many video understanding tasks such as action recognition [23,5] and video summarization [17]. However, nearly all networks are working as a black box. One typical example is that, when classifying two videos of swimming and basketball-playing, it is difficult to identify what elements are relied upon by an action recognition model, the scene information in the background or the action of the performer. Understanding the black-box characteristic of deep networks shows significant potential for analyzing failure cases, improving the model structure design, and even revealing shortcomings in the training data [32].

Since a neural network can be considered as a mapping from the input space to the output space, the task of understanding the network can be divided into two phases: 1) which part of the input is more utilized or is more important for the network; 2) how the mechanism inside the network derives the output, *i.e.*, the analytic derivation of this mapping function. The solution to the “which part” problem in the first phase is often referred to as **input attribution**

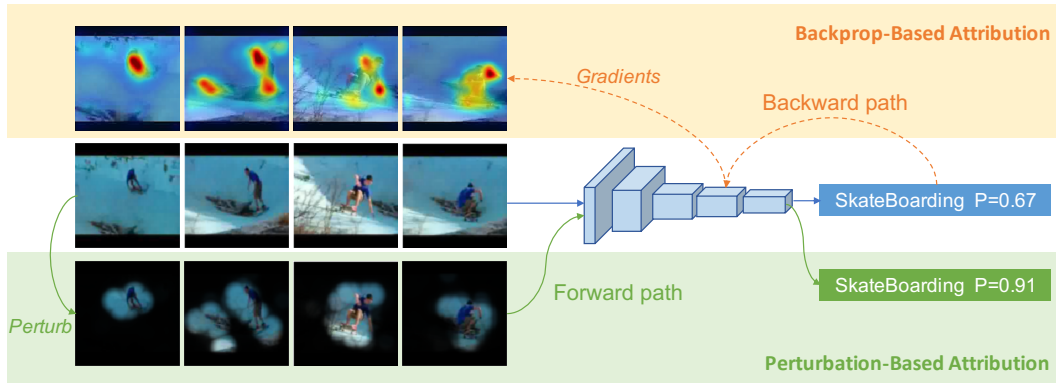


Fig. 1: Two approaches of visual explanation for deep neural networks. The upper block demonstrates the BP-based methods, which utilize gradients or modified gradients derived during the back-propagation to indicate the significance on the input frames. The lower one demonstrates the perturbation-based methods, which directly operates on the input and locates the area that affects the output most in a forward manner

method, *i.e.*, attributing the output of the network to the specific elements in a given input.

In contrast to the great progress of image attribution methods [32,26,24,33,19], there are only a few works reported for attribution methods aimed for videos. Sarah *et al.* [2] realized a visualization method (EB-R) to generate spatiotemporal saliency for CNN-RNN networks. As one class of attribution method general for any CNN-based network, Grad-CAM [19] and its variants [6,28] could also be applied on video attribution. However, problems are remaining. EB-R is short in generalization since it is specially designed for a certain structure. Grad-CAM is weak in capturing temporal importance on 3D-CNNs networks because the activation maps of the middle convolutional layer tends to lose some temporal sensitivity after passing through temporal pooling layers. Also, both of the two approaches are evaluated by subjective metrics which emphasize the consistency of attribution results with manual annotations or the human inspection. This deviates from the target of the attribution method, *i.e.*, finding the regions relied upon by models rather than humans.

In this paper, we focus on the attribution methods for spatial-temporal networks which take videos as input. Especially, we investigate the perturbation-based methods to fill its vacancy on video attribution task. As demonstrated in Fig. 1, backprop-based and perturbation-based attributions are two main categories of attribution methods. Comparing with backprop-based attributions that take gradients from the middle of networks, the perturbation-based method can treat the network completely as a black box since it only operates on the input and observes changes in the outputs. This makes the perturbation-based method applicable to diverse model structures for various video analysis tasks.

Specifically, our contributions can be summarized as follows:

- We fill in the vacancy of the perturbation-based approach under the video attribution task by extending the extremal perturbation method from 2D

(images) to 3D (videos). The proposed method, spatio-temporal perturbation, has no special restriction on model structures and can also generate spatio-temporal visual explanations.

- We shed light on objective evaluation metrics for video attribution methods by introducing two kinds of objective metrics as a complementary for the current subjective metric.
- We quantitatively evaluate and validate the spatio-temporal perturbation method’s effectiveness through extensive experiments.
- Our experiment provides the following important findings: 1) Attribution method tends to show opposite performances on objective and subjective metrics, that is, struggle between capturing “regions that people expect to pay attention to” and “information that models really care about” when predicting; 2) Adding the constraint of temporal consistency to the perturbation-based method can make the results perform well on subjective metrics (we designed a loss function that obtained the state-of-the-art results), but also accompanied by a decline in performance on objective metrics.

2 Related Works

2.1 Image Attribution Approaches

The goal of an image attribution method is to tell us which elements of the input (*e.g.*, pixels or regions for an image input) are responsible for its output (*e.g.*, the softmax probability for a target label in the image classification task). The results are commonly expressed as an importance map in which each scalar quantifies the contribution of the element in the corresponding position.

Backpropagation-based (BP-based) methods BP-based attribution approaches are established upon a common view that gradients (of the output with respect to the input) could highlight key regions in the input since they characterize how much variation would be triggered on the output by a tiny change on the input. [4] and [22] have shown the correlation between the pixels’ importance and their gradients for a target label. However, the importance map generated by raw gradients is typically visually noisy. The way to overcome this problem could be partitioned into three branches. DeConvNets [32] and Guided Backprop [26] modify the gradient of the ReLU function by discarding negative values during the back-propagation calculation. Integrated Gradients [29] and SmoothGrad [24] resist noises by accumulating gradients. LRP [3], DeepLift [20] and Excitation Backprop [33] propose modified backpropagation schemes by incorporating a local approximation or a probabilistic Winner-Take-All process. The BP-based method is highly efficient because it only needs one forward and backward pass to get the importance map for the input.

Activation-based methods Activation-based attribution approaches generate the importance map by linearly combining the activation maps output by

convolutional layer. Different methods vary in the choice of combining weights. CAM [34] selects parameters on the fully-connected layer as weights, while Grad-CAM [19] produces the weight by average pooling the gradients from the output to the activation. Grad-CAM++ [6] replaces the average pooling in Grad-CAM with coefficients calculated by second derivative.

Perturbation-based methods Perturbation-based attribution methods start from an intuitive assumption that the change of outputs could reflect the importance of certain elements when they are removed or keep only in the input. However, in order to find the optimal results, theoretically it is necessary to traverse the elements and their possible combinations in the input and observe their impact on the output. Due to the high time cost of this traversal process, how to obtain an approximate optimal solution faster is the research focus of this problem. Occlusion [32] and RISE [14] perturb an image by sliding a grey patch or randomly combining occlusion patches, respectively, and then use changes in the output as weights to sum different patch patterns. LIME [16] approximates networks into linear models and uses a super-pixel based occlusion strategy. Meaningful perturbation [11] converts the problem to an optimization task of finding a preservation mask that can maximize the output probability under the constraints of area ratio and smoothness. Real-time saliency [7] learns to predict a perturbation mask with a second neural network. Qi *et al.* [15] improved the optimization process by introducing integrated gradients and Wagner *et al.* [31] introduced certain restrictions in the optimization process to avoid adversarial results. Fong *et al.* [10] introduced extremal perturbations and special smooth masks to solve the problem of imbalance between several constraining terms.

2.2 Video Attribution Approaches

The goal of the video attribution is to obtain the regions taken important by a network of the input, in both spatial and temporal dimensions. The increase of dimension means inflated searching space and time cost. The attention has been attracted to adapt existing image attribution approaches for videos input. EB-R (excitation backprop for RNNs) [2] firstly extended the Excitation Backprop attribution method to the framework for videos, to be specific, the CNN-RNN structure. Grad-CAM [19] is naturally applicable to networks processing videos. [28] and [27] adapt activation-based methods for 3D convolutional networks to produce better visualization results over time. [12] presents a paradigm for generating importance maps for video models including 3D-CNNs and CNN-RNN. Differing from our method, the spatial and temporal maps are generated separately, by extended meaningful perturbation [11] and original Grad-CAM respectively.

2.3 Evaluation Methods for Attribution

Generally speaking, the quality of the importance map generated by different attribution methods is often evaluated from both subjective and objective as-

pects. The subjective aspect relies on human evaluation, that is, measurement from the perspective of human comprehension of the decision process. Methods tend to employ manual inspection and bounding box annotations for the object localization task. Especially, the Pointing Game [33] is one of the most commonly used metrics concerning simulating the object localization task. However, it is hard to guarantee that the decision process of deep networks are uniform with human's, which makes the subjective evaluations somewhat unreasonable. For objective evaluation, partial methods start from an input perturbation procedure [18,13,14], in which pixels are inserted or removed in order according to the importance they are arranged. The area under the curve (AUC) plotting changes of output softmax probability is adopted to assess importance maps. Starting from the common view that an ideal importance map should highlight small regions but contain as much as relevant information, Dabkowski *et al.*[8] proposed an entropy-based metric to quantify the amount of relevant information and the area of highlight regions. Montavon *et al.*[13] incorporated Explanation Continuity as a measure of assessment. Sanity check [1] proposed that if the result of an attribution method is independent of the training data and parameters of the model, this method is not an adequate method for model understanding.

3 Approach

In this section, we present the methodology for perturbation-based video attribution method. Let $\{x_t\}, t = 1, \dots, T$ represents a video consisting of T frames $x \in \mathbb{R}^{H \times W}$ with width W and height H , we investigate our attribution method on a deep model Φ that maps the image sequence to a softmax probability $\Phi_c(\{x_t\}) \in \mathbb{R}$ for a target class c . The goal of attribution methods is to derive a sequence of importance maps $\{m_t\}$ assigning to each pixel $x_{i,j,t}$ a value $m_{i,j,t}$. Here i, j refer to the spatial location of each pixel.

3.1 Perturbation-based attribution for videos

The aim of perturbation-based attribution is to find a reserving subset of the input, which is as small as possible while retaining the prediction accuracy on the target label. Based on this goal, we can also formulate the optimization target of the perturbation-based video attribution method as

$$\{m_t\}^* = \arg \min \left\{ \lambda \sum_{t=1}^T \|m_t\|_1 - \Phi_c(\{m_t \otimes x_t\}) \right\}, \quad (1)$$

where $\{m_t\}^*$ is the perturbation mask sequence which has the same shape as input frames $\{x_t\}$ and \otimes represents the local perturbation operation on the input frames according to the masks. To be specific, each pixel $x_{i,j,t}$ in frames is blurred by a Gaussian kernel if its corresponding mask value $m_{i,j,t} = 1$. Otherwise, it will remain unchanged. The first item in 1 constrains the number of pixels in videos selected by masks to be small. For convenience, we will call it the volume

of the masks. The second item encourages the model’s prediction accuracy to be retained.

However, if this formula is used directly as an optimization target, it often leads to the following problems: 1) The balance between the two terms of masks’ size and probability makes it difficult to obtain an optimal solution. A typical phenomenon is that optimization results vary according to the value of λ . 2) It is easy to produce adversarial results, which makes the method lose its explanation to the model. To solve this problem, other terms can be introduced into the optimization target, e.g., to limit the smoothness of the masks’ shape, however, this will further exacerbate the trade-off problem.

In order to avoid the above problems, we transform the optimization target into an extremal perturbation form according to [10]. We firstly find a sequence of masks that maximizes the model’s probability under a constrained perturbation size as

$$\{m_t\}_V = \arg \max_{\{m_t\}: \sum_{t=1}^T \|m_t\|_1 = V} \{\Phi_c(\{m_t \otimes x_t\})\} \quad (2)$$

in which V represents the volume of perturbed parts. The second step is to set the lowest bound for the output probability Φ_0 , and search for the smallest mask sequence achieving this bound after enumerating several constraining sizes of masks. That is to say, finding the smallest size choice V^* as below:

$$V^* = \min \{V : \Phi_c(\{m_t \otimes x_t\}) \geq \Phi_0\}, \quad (3)$$

and set $\{m_t\}_{V^*}$ as the extremal solution.

We solve the optimization in Eq. 2 by Stochastic Gradient Descent method and relax the values in masks to be continuous number in full range of $[0, 1]$. In order to constrain the masks’ volume approaching the setting target volume V , we change the first item in Eq. 2 to be a loss function that regularizes the top- V values in masks closing to 1 and the remaining values to 0. Formally it could be represented as below

$$\{m_t\}_V = \arg \min \left\{ \lambda \|\text{vecsort} \{m_t\} - \mathbf{r}_V\|^2 - \Phi_c(\{m_t \otimes x_t\}) \right\}, \quad (4)$$

where $\text{vecsort} \{m_t\} \in \mathbb{R}^{T \times H \times W}$ is a vector containing all values in masks sorted in ascending order and \mathbf{r}_V is template vector consisting of $(1 - V) \times T \times H \times W$ zeros followed by $V \times T \times H \times W$ ones.

3.2 Mathematical analysis

In the following, we will analyze the optimization process of extreme perturbation when using a gradient-based method.

The Eq. 2 decides that the value of $m_{i,j,t}$ will be updated for every time’s backward by a gradient

$$\Delta m_{i,j,t} = \begin{cases} \ell \left(2\lambda m_{i,j,t} - \frac{\partial \Phi_c(m \otimes x)}{\partial ((m \otimes x)_{i,j,t})} x_{i,j,t} \right) & m_{i,j,t} \notin \text{top}V(\{m_t\}), \\ \ell \left(2\lambda (m_{i,j,t} - 1) - \frac{\partial \Phi_c(m \otimes x)}{\partial ((m \otimes x)_{i,j,t})} x_{i,j,t} \right) & m_{i,j,t} \in \text{top}V(\{m_t\}) \end{cases}, \quad (5)$$

where ℓ denotes the learning rate and $\text{top}V(\{m_t\})$ denotes the set formed by the first V large values in $\{m_t\}$.

For the first V large mask values, they will obtain more updates than those not sorted into the first V rank. The update value is determined by the magnitude of the mask value itself, as well as the contribution of the covered pixel to the model’s prediction which is obtained from the product of the pixel value and its gradient ($\text{Gradient} \odot \text{Input}$, where \odot is Hadamard product indicating element-wise product). Actually, the Hadamard product of the input and the gradient is widely utilized to generate visual explanation in gradient-based attribution [21]. Eq. 5 shows us a positive feedback process, that is, those important pixels with large $\text{Gradient} \odot \text{Input}$ values tend to be arranged higher mask values, so that they will be retained in the next iteration and get a higher gradient.

3.3 Metrics for Video Attribution

The quantitative evaluation used in many previous attribution methods [19,2] often relies on subjective human inspection or manual annotations. For example, the bounding boxes grounding the target object or action categories are required by Pointing Game (PG) [33], one commonly exploited metric. However, these subjective metrics may become impractical in video cases since annotating the ground-truth classes frame by frame is labor-intensive and time-consuming. Also, the bounding boxes for some actions are ambiguous even for humans. Therefore, we introduce the following objective metrics as supplements for the evaluation of video attribution methods.

Causal Metric (Insertion and Deletion) The principle of the causal metric is to add pixels to a blank video (insertion) or to remove pixels from the original video (deletion), both in an order decided by the pixels’ importance [14,18,13]. After each insertion or deletion is performed, the output probability is then continuously computed and finally, a curve recording the probability changes can be generated. The area under the curve (AUC) is considered to indicate the correctness of the validated sequence of importance maps. Ideally, an accurate importance map sequence would cause the curve to rise significantly and then keep at a high probability in the insertion mode. In contrast, in the deletion mode, a sharp decline would be observed and then the curve would remain at a low value. Causal metric obtains a quantized value between 0 and 1. For insertion, the greater the value, the better the result; For deletion, the less the value, the better the result.

Saliency Metric We further introduce the saliency metric proposed in [7], which is a well correspondent with the objective of importance maps generation that the network is supposed to be able to retain the correct prediction from the preserved region and simultaneously the region’s area should be as small as possible. Originally, [7] proposes to find the tightest rectangular crop that contains the entire salient region as the input in order to prevent potential adversarial

artifacts. However, in the case of video, this often results in a cuboid that almost fills the entire spatial and temporal space so that the area factor does not work anymore (close to 1). Thus, here we focus back on the salient region itself and use its own area instead of the tightest box. The metric can be calculated as

$$\text{SM} = \log(\max(a, \tau)) - \log(p_c), \quad (6)$$

where a is the area fraction of the importance map, τ is the threshold in order to prevent instabilities at low area fractions, p_c is the probability of the target class c returned by the network based on the masked region. As mentioned in [7], the measure can be regarded as the relative amount of information between the output probability and the concentration of the masked region following the information theory. Note that the metric may give potentially negative values for a good saliency detector.

4 Experiments and Results

4.1 Experiments setting

Different from existing approaches for video attribution, our approach has no requirement on the network structures. To analyze the explanation of our approach on networks taking videos as input, we applied it on two kinds of widely used model structures: CNN-RNN and 3D-CNNs. Specifically, we select two networks of VGG16-LSTM [2] and R(2+1)D [30], which are the representative networks under the two model structures. We validated attribution methods with the model structures on subsets of two video datasets: UCF101-24 and EPIC-Kitchens since the bounding box annotations are (partially) available on them.

UCF101 Dataset UCF101-24 [25] is a subset of UCF101 dataset. It contains 3207 videos belonging to 24 classes that are intensively labeled with spatial bounding box annotations of humans performing actions. In our experiment, we trained a VGG16-LSTM network and an R(2+1)D network on the UCF101-24 dataset by the training set defined in THUMOS13. To generate importance maps for evaluating attribution methods, we randomly selected 5 videos on each category to form a test set with 120 videos.

EPIC-Kitchens Dataset EPIC-Kitchens [9] is a dataset for egocentric video recognition. 39596 video clips segmented from 432 long videos are provided in the dataset, along with action and object labels. We choose the top 20 classes with the most number of clips to form the EPIC-Object and EPIC-Action sub-datasets, and randomly selected 5 clips for each class to generate two test sets and used the remained clips to train models. Bounding boxes for the ground-truth objects in EPIC-Objects are provided in 2fps. On the EPIC-Action task, we connect a randomly selected part of each clip with its adjacent background frame sequence, to form a set for testing the temporal localization performance of attribution methods.

Model Training We trained a VGG16-LSTM model and an R(2+1)D model on every classification task. We use VGG16-LSTM networks from [2] and fine-tune the fully-connected (FC) layers and LSTM layer on specific datasets. To avert the gradient vanishing, we block the gradient propagation on hidden states and take the average of outputs on all-time steps as the final prediction. For the R(2+1)D network, we use R(2+1)D-18 structure [30] and only fine-tune their final convolutional block and the FC layer. Both in training and testing phases, we sample 16 frames as the input by splitting one video clip into 16 segments and selecting one frame in each split. The classification accuracy for each network on every task’s test set is shown in 1. Notably, the accuracy on the UCF101-24 test set is nearly 100%. We think this is due to the models are pre-trained on the UCF101 datasets.

Table 1: Top1 & 5 classification accuracy of our test networks on 2 datasets (3 tasks)

Acc. (Top1/Top5)	UCF101-24	EPIC-Objects	EPIC-Actions
R(2+1)D	100% (100%)	57% (85%)	77% (97%)
VGG16-LSTM	97.5% (100%)	55% (84%)	81% (100%)

Evaluation Metrics We adopt three evaluation metrics introduced in Sec. 3.3:

- **Pointing Game:** We select the pointing game metric to evaluate whether the importance maps generated by an attribution method could locate the “key” spatial regions or temporal segments, which is called spatial pointing game (**S-PT**) and temporal pointing game (**T-PT**) respectively. We perform the S-PT evaluation on the UCF101-24 and EPIC-Object test sets. Following [2], we set a tolerance radius of 7-pixel, *i.e.*, one hit is recorded if a 7-pixel radial circle around the maximum point in an importance map intersects the ground-truth bounding box. On the EPIC-Action test set, we evaluate methods by the T-PT metric, in which a hit is recorded only when the index of the frame with the highest importance value locates in the ground-truth segment.
- **Causal Metric:** We report both the insertion (**CI**) and deletion metrics (**CD**) in our experiment. As recommended by [14], we insert pixels into an empty video with highly blurred frames and remove pixels to gray level when deleting them.
- **Saliency Metric:** The metric is computed using the binaralized importance map with threshold 0.50 and 0.75, denoting S_{50} and S_{75} , respectively. As for the threshold τ used in Eq. 6, we follow [7] and use 0.05.

Implementation details Following [10], all masks are generated and optimized based on smaller seed masks $\bar{m}_t \in \mathbb{R}^{\bar{H} \times \bar{W} \times T}$ and in our experiment we set $H = 7\bar{H}$ and $W = 7\bar{W}$. The seed masks are then up-sampled by the transposed convolution operation with the smooth max kernel defined in [10]. We report our quantitative results on the summed masks generated under volume constraints of 0.01, 0.05, 0.1.

4.2 Comparison of attribution methods

We compare with several baseline methods to validate the effectiveness of our proposed approach. Since we are the first to apply the perturbation-based attribution method on spatiotemporal networks, we firstly compare our method with a vanilla extremal perturbation approach in which each frame is assigned the same area constraint. However, considering the optimization process, there could be two variances for this vanilla extension: searching for masks of all frames together (noted as **Extm. Ptb. Sync.**), or separately optimizing each frame’s mask (noted as **Extm. Ptb. Unsync.**). In the extremal perturbation unsync. setting, when searching for the m_t , all the other masks $\{m_{t'}\}_{t' \neq t}$ are set to zeros to guarantee the maximum response of the model on the single frame.

We also use three more baseline methods to evaluate the effectiveness of our spatial attention module.

- **Grad-CAM**[19]: A generalized attribution method that could be utilized on both 3D-CNNs and CNN-RNN networks. For the R(2+1)D model, we extract generate the heatmaps of the last 3d convolutional layer and upsample the maps to the shape of input images, in both spatial and temporal dimension. For the VGG16-LSTM model, the heatmaps are generated on the *conv5* VGG16.
- **Saliency Tubes**[28]: A visualization method specially designed for 3D-CNNs networks. The activation maps of the last 3d convolutional layer are combined by weights in the final FC layer to produce heatmaps. We upsample the maps as in Grad-CAM.
- **EB-R**[2]: A backprop-based method designed for CNN-RNN structures which uses a modified back-propagation algorithm. We adopt it directly on our VGG16-LSTM models and capture the heatmaps for each frames at *conv5* layer of VGG16.

Visualization results comparison Fig. 2 and Fig. 3 visualize the importance maps generated by our approach compared with baseline methods. On both the R(2+1)D and VGG16-LSTM models, our method is inclined to assign a high percentage of importance on the first frame and the last frame is also taken important by our method on the R(2+1)D model. This is reasonable and consistent with our analysis in Sec. 3.2. For example, in VGG16-LSTM, when the outputs are averaged on all-time steps and backward gradients on hidden states are blocked, the input frame of the first time step tends to be assigned higher gradients since it is combined with a hidden state initialized by zero. Moreover, on both figures, we can observe that the regions preserved by perturbation-based methods show consistency with the gradient-based methods, which also proves our analysis in Sec. 3.2, that is, the extremal perturbation method continuously intensifies focuses on regions with high gradient responses by iterations. More visualization results could be found in the supplementary materials.

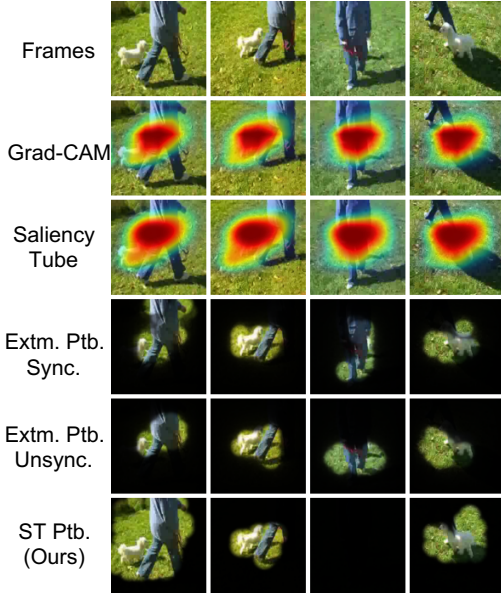


Fig. 2: Comparison of visualization results generated on a UCF101-24 video with ground-truth of “WalkingWith-Dog” to explain the R(2+1)D model.

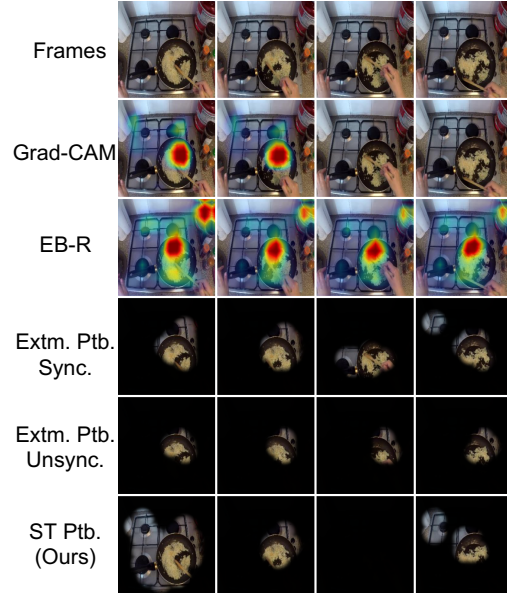


Fig. 3: Comparison of visualization results generated on a EPIC video with ground-truth object label of “Pan” to explain the VGG16-LSTM model.

Quantitative results comparison Since the causal metric and saliency metric are firstly introduced into the video attribution task, to explore their lower and upper bounds, we first test them with masks of random values. We list the result in Tab. 2 and Tab. 3. The random masks get the worst performance on nearly all metrics except for the deletion causal metric (CD). We suspect the reason to be that the random deletion of pixels or regions from the image sequence tends to generate the adversarial input, which will drastically decrease the model’s prediction accuracy. We have also tried other paradigms of deletion, including replacing pixels’ values to their blurred values rather than gray, or removing patches instead of pixels, but the random masks still tend to perform low CD values. According to this reason, we will not consider the results on this metric too much in the following part of this paper.

Table 2: Quantitative evaluation based on R(2+1)D networks

Methods	EPIC-Object					UCF101-24				
	PG↑	CI↑	CD↓	S ₅₀ ↓	S ₇₅ ↓	PG↑	CI↑	CD↓	S ₅₀ ↓	S ₇₅ ↓
Random	-	10.9	6.1	8.86	8.14	-	29.1	18.0	1.83	1.94
Grad-CAM[19]	7.1	39.3	7.5	3.57	4.15	47.5	77.6	30.7	-0.38	0.33
Saliency Tubes[28]	6.6	35.9	8.9	3.39	4.51	41.4	76.9	32.1	-0.37	0.49
Extm. Ptb. Sync.	7.0	37.0	7.2	4.45	3.34	45.2	85.0	25.0	0.02	0.33
Extm. Ptb. Unsync.	7.1	30.2	8.0	4.65	3.34	42.8	80.3	29.3	0.17	0.52
ST Ptb. (Ours)	6.7	42.3	7.7	2.97	2.65	46.8	89.5	24.8	-0.65	-0.46

For the R(2+1)D network, our method gets the best results on all objective metrics, which means the method could effectively locate the key regions relied on by the networks no matter datasets. Our method could also achieve competitive

Table 3: Quantitative evaluation based on VGG16-LSTM networks

Methods	EPIC-Object					UCF101-24				
	PG \uparrow	CI \uparrow	CD \downarrow	$S_{50}\downarrow$	$S_{75}\downarrow$	PG \uparrow	CI \uparrow	CD \downarrow	$S_{50}\downarrow$	$S_{75}\downarrow$
Random	-	25.5	10.7	5.24	3.92	-	53.9	21.9	5.52	5.28
Grad-CAM[19]	6.1	45.0	13.9	1.42	1.53	35.5	82.9	37.9	0.55	0.65
EB-R [2]	6.9	39.6	11.5	2.59	1.67	46.5	81.2	20.3	2.38	1.14
Extm. Ptb. Sync.	5.9	54.9	10.5	2.40	3.25	41.5	89.0	21.2	1.62	2.06
Extm. Ptb. Unsync.	6.2	47.0	11.6	1.92	1.88	39.9	84.6	23.1	2.18	2.67
ST Ptb. (Ours)	5.9	53.7	12.0	0.91	0.64	40.0	89.2	21.9	0.91	1.30

performance on objective metrics tested by VGG16-LSTM networks. On the VGG16-LSTM model trained by UCF101-24 dataset, Grad-CAM’s masks get striking results on the S_{50} and S_{70} metrics but not on the CI metric. From the visualization results, we find that although values in masks generated by Grad-CAM are small in general, there tend to show very high and sharp peaks on some masks. This results in the cropping regions to be very small, but still contain useful information that causes the model to be highly responsive.

Another noteworthy phenomenon shown in the tables is that although the perturbation-based methods perform well under objective metrics, they have not achieved significant results under the subjective metric of PG. We consider two reasons as an explanation. First, compared to the backprop-based method, the values in masks generated by the perturbation method are regularized to be close to 0 or 1, which makes the maximum point on the mask ambiguous. Second, the PG metric mainly quantifies whether the masks generated by a method are consistent with human judgment. However, the purpose of the attribution method is to find the input regions that are focused on networks for prediction. Whether the importance map produced by one attribution method is close to the manual annotation or not is not only determined by the method, but also by the characteristics of the model itself.

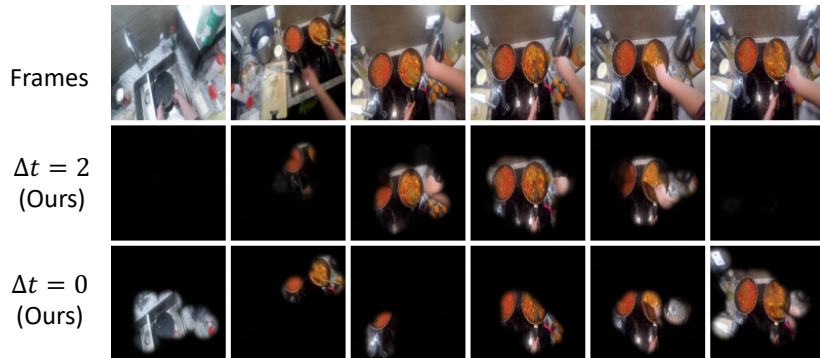


Fig. 4: Visualization of perturbation masks on R(2+1)D for an EPIC-Action video. The left part of the video is a background clip.

4.3 Is the constraint on temporal consistency needed?

One natural idea for designing the attribution method of spatio-temporal networks is to artificially introduce operations that constrain the temporal consistency in the optimization process of perturbation. To explore the potential effectiveness of the intervention to the temporal consistency, we designed two kinds of operations: smoothing masks in time and adding special loss to control the shape of generated masks.

Table 4: Evaluation results on EPIC-Action test set

Methods	R(2+1)D			VGG16-LSTM		
	T-PG↑	CI↑	CD↓	T-PG↑	CI↑	CD↓
EB-R	-	-	-	0.57	14.3	37.5
$\Delta t=0$ (Ours)	0.33	59.3	17.5	0.37	49.9	12.4
$\Delta t=1$ (Ours)	0.44	53.2	20.8	0.57	35.4	22.3
$\Delta t=2$ (Ours)	0.48	52.2	22.0	0.55	34.9	23.7
$\Delta t=3$ (Ours)	0.47	51.3	23.6	0.55	34.8	24.2

Temporal smoothness of masks We exploit a simple Gaussian kernel k to smooth the value of $m_{i,j,t}$ on masks according to values of its neighbours in temporal dimension to $m'_{i,j,t}$

$$m'_{i,j,t} = Z^{-1} \sum_{t'=t-\Delta t}^{t+\Delta t} k(t'-t)m_{i,j,t'} \quad (7)$$

where Z normalizes the kernel to sum to one. The kernel k is a radial basis function with profile $k(u) = \exp(-u^2/(0.6\sigma))$ and set $\sigma = \Delta t$ to ensure the kernel's sharpness. We add this temporal smoothness operator to our spatio-temporal perturbation method and test its effectiveness by choosing three different values of Δt on the EPIC-Action recognition task. Moreover, our proposed method could be seen as the case of $\Delta t = 0$. As shown in Tab. 4 and Fig. 4, after adding the smoothness operators, although the visualization results and the performance on the temporal pointing game is improved, the results on causal metrics become worse. The result is consistent with what we analysed for Tab. 2 and Tab. 3, i.e., attribution methods tend to produce an opposite performance on objective and subjective metrics. We think this phenomenon could be avoided if the spatio-temporal network could be completely designed and fully trained.

Constraining the shape of mask One way to constrain mask temporally is to use higher-order differences between frames as an energy function, *e.g.*, using 2nd-order differences to control the smoothness. However, it would be more likely to generate a mask without an obvious difference in the temporal dimension as the constraint seems too strong. Another intuitive idea for generating masks consistent both spatially and temporally is to guarantee that the high-value pixels of the mask can be clustered into some certain area with a specific shape

in the joint spatial and temporal space. Here we introduce a special loss function L_K that aims to gather high-value pixels into some pre-defined shape by doing 3D convolution on the importance maps $M = \{m_t\}$. The K in L_K denotes the kernel used in convolution, which satisfies $K \in \{0, 1\}^{(H_K+1) \times (W_K+1) \times (T_K+1)}$. The loss function can be defined as follows,

$$L_K(M) = (\max(M * K) - \sum_{i,j,t} K_{i,j,t})^2, \quad (8)$$

where $*$ denotes 3D convolution. The loss can be regarded as a weak supervision (since only area with max value contributes the loss) that guides the mask to concentrate. In the experiment, we use a ellipsoid kernel which defined as follows, $\forall i \in \{0, \dots, H_K\}, j \in \{0, \dots, W_K\}, t \in \{0, \dots, T_K\}$,

$$K_{i,j,t} = \begin{cases} 0, & \sqrt{(\frac{i}{H_K} - 0.5)^2 + (\frac{j}{W_K} - 0.5)^2 + (\frac{t}{T_K} - 0.5)^2} > 1; \\ 1, & \text{otherwise.} \end{cases} \quad (9)$$

Table 5: Evaluation results of constraining the shape of mask by loss function

L_K Networks	Methods	EPIC-Object					UCF101-24				
		PG \uparrow	CI \uparrow	CD \downarrow	S ₅₀ \downarrow	S ₇₅ \downarrow	PG \uparrow	CI \uparrow	CD \downarrow	S ₅₀ \downarrow	S ₇₅ \downarrow
R(2+1)D	Ours	6.7	42.3	7.7	2.97	2.65	46.8	89.5	24.8	-0.65	-0.46
	Ours+Loss	8.5	36.2	8.5	2.80	3.35	56.0	83.3	35.1	-0.09	0.31
VGG16-LSTM	Ours	5.9	53.7	12.0	0.91	0.64	40.0	89.2	21.9	0.91	1.30
	Ours+Loss	9.2	40.6	13.1	1.11	1.55	53.0	82.8	24.6	1.11	0.77

The quantitative results after adding the loss function of our method are shown in Tab. 5. The loss function significantly improved the performance of our method on the PG metric, which even obtains the state-of-the-art results comparing with baseline methods. But the method produces opposite performance on objective metrics, which is similar to the results shown above.

5 Conclusion

In this paper, we focus on the attribution methods for spatio-temporal networks and provide a study of the existing methods. We have presented the spatio-temporal perturbation (ST perturbation) method, a new perturbation-based method for attributing deep spatio-temporal networks and generating visual explanations. We extend the extremal perturbation method from 2D (images) to 3D (videos) and the mathematical discussion and experimental results show that the simple extension could generate competitive results. To evaluate different methods for video attribution objectively, we introduced two kinds of metrics: causal metrics (deletion and insertion) and saliency metrics. We conducted extensive experiments on three datasets multiplied with two models and confirmed that ST perturbation obtains competitive results on the newly introduced objective metrics. In addition, we explored two ways of constraining the temporal consistency on ST perturbation and observed improvements on subjective metrics by adding each. Interestingly, we find that attribution methods tend to perform oppositely on objective and subjective metrics.

References

1. Adebayo, J., Gilmer, J., Muelly, M., Goodfellow, I., Hardt, M., Kim, B.: Sanity checks for saliency maps. In: *Advances in Neural Information Processing Systems*. pp. 9505–9515 (2018)
2. Adel Bargal, S., Zunino, A., Kim, D., Zhang, J., Murino, V., Sclaroff, S.: Excitation backprop for rnns. In: *Proceedings of the IEEE Conference on Computer Vision and Pattern Recognition (CVPR)*. pp. 1440–1449 (2018)
3. Bach, S., Binder, A., Montavon, G., Klauschen, F., Müller, K.R., Samek, W.: On pixel-wise explanations for non-linear classifier decisions by layer-wise relevance propagation. *PloS one* **10**(7) (2015)
4. Baehrens, D., Schroeter, T., Harmeling, S., Kawanabe, M., Hansen, K., MÄzler, K.R.: How to explain individual classification decisions. *Journal of Machine Learning Research* **11**(Jun), 1803–1831 (2010)
5. Carreira, J., Zisserman, A.: Quo vadis, action recognition? a new model and the kinetics dataset. In: *proceedings of the IEEE Conference on Computer Vision and Pattern Recognition*. pp. 6299–6308 (2017)
6. Chattopadhyay, A., Sarkar, A., Howlader, P., Balasubramanian, V.N.: Grad-cam++: Generalized gradient-based visual explanations for deep convolutional networks. In: *IEEE Winter Conference on Applications of Computer Vision (WACV)*. pp. 839–847 (2018)
7. Dabkowski, P., Gal, Y.: Real time image saliency for black box classifiers. In: *Advances in Neural Information Processing Systems*. pp. 6967–6976 (2017)
8. Dabkowski, P., Gal, Y.: Real time image saliency for black box classifiers. In: *Advances in Neural Information Processing Systems*. pp. 6967–6976 (2017)
9. Damen, D., Doughty, H., Maria Farinella, G., Fidler, S., Furnari, A., Kazakos, E., Moltisanti, D., Munro, J., Perrett, T., Price, W., et al.: Scaling egocentric vision: The epic-kitchens dataset. In: *Proceedings of the European Conference on Computer Vision (ECCV)*. pp. 720–736 (2018)
10. Fong, R., Patrick, M., Vedaldi, A.: Understanding deep networks via extremal perturbations and smooth masks. In: *Proceedings of the IEEE International Conference on Computer Vision (ICCV)*. pp. 2950–2958 (2019)
11. Fong, R.C., Vedaldi, A.: Interpretable explanations of black boxes by meaningful perturbation. In: *Proceedings of the IEEE International Conference on Computer Vision (ICCV)*. pp. 3429–3437 (2017)
12. MänttÄri, J., Broomé, S., Folkesson, J., Kjellström, H.: Interpreting video features: a comparison of 3d convolutional networks and convolutional lstm networks. *arXiv preprint arXiv:2002.00367* (2020)
13. Montavon, G., Samek, W., Müller, K.R.: Methods for interpreting and understanding deep neural networks. *Digital Signal Processing* **73**, 1–15 (2018)
14. Petsiuk, V., Das, A., Saenko, K.: Rise: Randomized input sampling for explanation of black-box models. In *British Machine Vision Conference (BMVC)* (2018)
15. Qi, Z., Khorram, S., Li, F.: Visualizing deep networks by optimizing with integrated gradients. In: *Proceedings of the IEEE Conference on Computer Vision and Pattern Recognition Workshops (CVPRW)*. pp. 1–4 (2019)
16. Ribeiro, M.T., Singh, S., Guestrin, C.: ” why should i trust you?” explaining the predictions of any classifier. In: *Proceedings of the 22nd ACM SIGKDD international conference on knowledge discovery and data mining*. pp. 1135–1144 (2016)
17. Rochan, M., Ye, L., Wang, Y.: Video summarization using fully convolutional sequence networks. In: *Proceedings of the European Conference on Computer Vision (ECCV)*. pp. 347–363 (2018)

18. Samek, W., Binder, A., Montavon, G., Lapuschkin, S., Müller, K.R.: Evaluating the visualization of what a deep neural network has learned. *IEEE transactions on neural networks and learning systems* **28**(11), 2660–2673 (2016)
19. Selvaraju, R.R., Cogswell, M., Das, A., Vedantam, R., Parikh, D., Batra, D.: Grad-cam: Visual explanations from deep networks via gradient-based localization. In: *Proceedings of the IEEE international conference on computer vision*. pp. 618–626 (2017)
20. Shrikumar, A., Greenside, P., Kundaje, A.: Learning important features through propagating activation differences. In: *Proceedings of the 34th International Conference on Machine Learning (ICML)*. pp. 3145–3153 (2017)
21. Shrikumar, A., Greenside, P., Kundaje, A.: Learning important features through propagating activation differences. In: *Proceedings of the 34th International Conference on Machine Learning-Volume 70*. pp. 3145–3153. *JMLR. org* (2017)
22. Simonyan, K., Vedaldi, A., Zisserman, A.: Deep inside convolutional networks: Visualising image classification models and saliency maps. *arXiv preprint arXiv:1312.6034* (2013)
23. Simonyan, K., Zisserman, A.: Two-stream convolutional networks for action recognition in videos. In: *Advances in neural information processing systems*. pp. 568–576 (2014)
24. Smilkov, D., Thorat, N., Kim, B., Viégas, F., Wattenberg, M.: Smoothgrad: removing noise by adding noise. *arXiv preprint arXiv:1706.03825* (2017)
25. Soomro, K., Zamir, A.R., Shah, M.: Ucf101: A dataset of 101 human actions classes from videos in the wild. *arXiv preprint arXiv:1212.0402* (2012)
26. Springenberg, J., Dosovitskiy, A., Brox, T., Riedmiller, M.: Striving for simplicity: The all convolutional net. In: *ICLR (workshop track)* (2015)
27. Stergiou, A., Kapidis, G., Kalliatakis, G., Chrysoulas, C., Poppe, R., Veltkamp, R.: Class feature pyramids for video explanation. *arXiv preprint arXiv:1909.08611* (2019)
28. Stergiou, A., Kapidis, G., Kalliatakis, G., Chrysoulas, C., Veltkamp, R., Poppe, R.: Saliency tubes: Visual explanations for spatio-temporal convolutions. In: *2019 IEEE International Conference on Image Processing (ICIP)*. pp. 1830–1834 (2019)
29. Sundararajan, M., Taly, A., Yan, Q.: Axiomatic attribution for deep networks. In: *Proceedings of the 34th International Conference on Machine Learning (ICML)*. pp. 3319–3328 (2017)
30. Tran, D., Wang, H., Torresani, L., Ray, J., LeCun, Y., Paluri, M.: A closer look at spatiotemporal convolutions for action recognition. In: *Proceedings of the IEEE conference on Computer Vision and Pattern Recognition*. pp. 6450–6459 (2018)
31. Wagner, J., Kohler, J.M., Gindele, T., Hetzel, L., Wiedemer, J.T., Behnke, S.: Interpretable and fine-grained visual explanations for convolutional neural networks. In: *Proceedings of the IEEE Conference on Computer Vision and Pattern Recognition (CVPR)*. pp. 9097–9107 (2019)
32. Zeiler, M.D., Fergus, R.: Visualizing and understanding convolutional networks. In: *European conference on computer vision (ECCV)*. pp. 818–833 (2014)
33. Zhang, J., Bargal, S.A., Lin, Z., Brandt, J., Shen, X., Sclaroff, S.: Top-down neural attention by excitation backprop. *International Journal of Computer Vision* **126**(10), 1084–1102 (2018)
34. Zhou, B., Khosla, A., Lapedriza, A., Oliva, A., Torralba, A.: Learning deep features for discriminative localization. In: *Proceedings of the IEEE conference on computer vision and pattern recognition (CVPR)*. pp. 2921–2929 (2016)

A Comprehensive Study on Visual Explanations for Spatio-temporal Networks (Supplementary Material)

Anonymous ECCV submission

Paper ID 4702

In this supplementary material, we provide S1. visualization results for video attribution, S2. causal metric evaluation results by patch wise paradigm and S3. recognition accuracy on masked videos.

S1. Visualization results for video attribution We demonstrate more qualitative visualization results in videos. The video can be found in the attached file. The video consists of two parts: comparisons of attribution methods and investigation of temporal consistency constraints, which correspond to Section 4.2 and Section 4.3 in the main submission, respectively.

S2. Causal metric evaluation results by patch-wise paradigm As noted in Section 4.1 (Quantitative results comparison), we evaluate different video attribution methods by insertion and deletion causal metrics (CI and CD) with the pixel-wise paradigm [?]. Here, to avoid the potential adversarial input caused by pixel-wise insertion/deletion, we show the evaluation results in Tab.1 and Tab.2 with the patch-wise paradigm, *i.e.*, inserting or deleting patches from frames with the order decided by the average values on their corresponding patches of masks. In our experiments, we divide each frame into 16×16 patches. Generally, the results on the two paradigms are consistent. For example, for CI, our ST Perturbation method always tend to get the best or competitive results on the two kinds of networks. For CD, the random masks still show low numerical results although there are some increases on the patch-wise paradigm.

Table 1: Causal metrics results with pixel-wise and patch-wise paradigms on R(2+1)D networks

Methods	EPIC-Object				UCF101-24			
	Pixel-wise		Patch-wise		Pixel-wise		Patch-wise	
	CI \uparrow	CD \downarrow	CI \uparrow	CD \downarrow	CI \uparrow	CD \downarrow	CI \uparrow	CD \downarrow
Random	10.9	6.1	16.8	9.8	29.1	18.0	49.6	19.6
Grad-CAM[?]	39.3	7.5	37.2	9.6	77.6	30.7	80.1	31.9
Saliency Tubes[?]	35.9	8.9	36.3	11.3	76.9	32.1	79.8	32.0
Extm. Ptb. Sync.[?]	37.0	7.2	35.9	9.8	85.0	25.0	87.2	35.7
Extm. Ptb. Unsync.[?]	30.2	8.0	31.2	9.4	80.3	29.3	78.7	38.4
ST Ptb. (Ours)	42.3	7.7	45.7	8.5	89.5	24.8	93.1	31.6

Table 2: Causal metrics results with pixel-wise and patch-wise paradigms on VGG16LSTM networks

Methods	EPIC-Object				UCF101-24			
	Pixel-wise		Patch-wise		Pixel-wise		Patch-wise	
	CI \uparrow	CD \downarrow	CI \uparrow	CD \downarrow	CI \uparrow	CD \downarrow	CI \uparrow	CD \downarrow
Random	25.5	10.7	30.6	16.4	53.9	21.9	63.0	25.9
Grad-CAM[?]	45.0	13.9	49.3	15.7	82.9	37.9	83.5	41.9
EB-R[?]	39.6	11.5	39.7	12.9	81.2	20.3	82.0	20.4
Extm. Ptb. Sync.[?]	54.9	10.5	54.5	12.5	89.0	21.2	89.3	21.5
Extm. Ptb. Unsync.[?]	47.0	11.6	47.5	12.7	84.6	23.1	85.1	23.1
ST Ptb. (Ours)	53.7	12.0	53.5	13.4	89.2	21.9	89.2	22.9

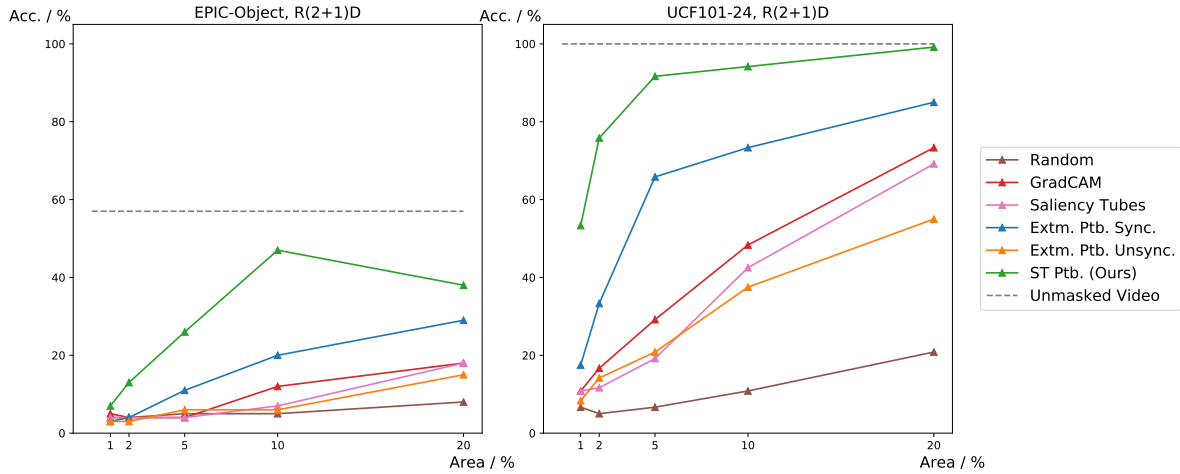


Fig. 1: Recognition accuracy on R(2+1)D with masked videos. The masked videos are generated by retaining only the first x (x is the tick value of the horizontal axis) percent of pixels in the video.

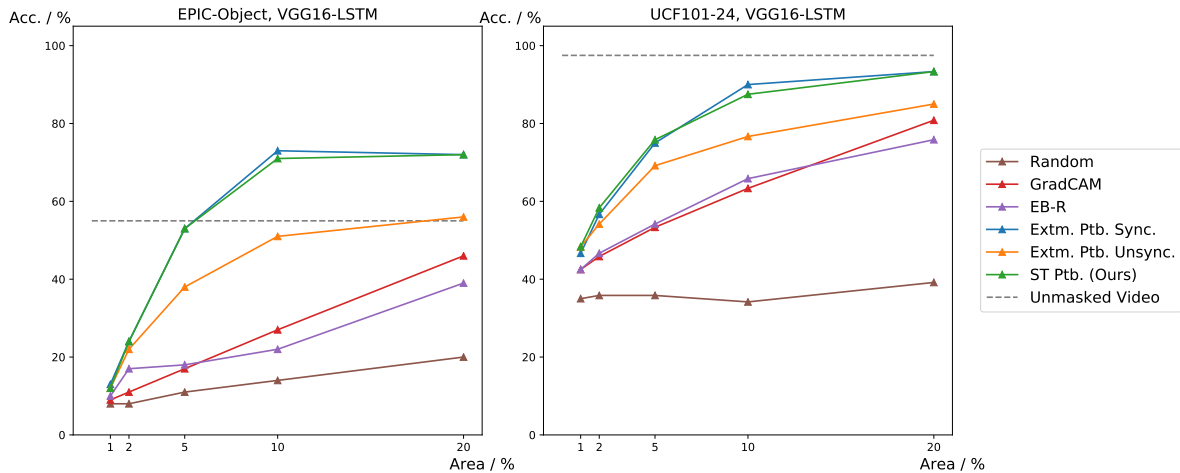


Fig. 2: Recognition accuracy on VGG16LSTM with masked videos. The masked videos are generated by retaining only the first x percent (x is the tick value of the horizontal axis) of pixels in the video.

S3. Recognition accuracy on masked videos As we mentioned in the main text, the goal of video attribution is to find a reserving subset of the input, whose size should be as small as possible while retaining the prediction accuracy on the target label. For a given input video and its corresponding masks, we generate a masked video by preserving only the pixels assigned with high mask values. According to the goal of video attribution, a good attribution method could produce masked videos with high recognition accuracy by its masks. We experimentally investigate the relationship between recognition accuracy and masks generated by different attribution methods in following and the results are demonstrated in Fig 1 and Fig 2. We generate five perturbed videos from each video by respectively preserving only the first 1%, 2%, 5%, 10%, and 20% pixels with the highest mask values and blurring the remained pixels. The accuracy of unmasked videos are shown in grey dotted line. Also, to investigate the lower bound of the accuracy change curve, we report the results of perturbed videos generated according to random masks.

It can be seen from Fig 1 and Fig 2 that in any case, our method could achieve the highest accuracy (or comparable to Extm. Ptb. Sync.) and outperform the other methods by a significant margin, which demonstrates that our method could discover pixels that are critical for recognition. For VGG16LSTM models, Extm, Ptb. Sync. get the nearly same accuracy as our method, we think of the reason to be that on VGG16LSTM model our method tend to allocate the preservation regions with nearly equal size on every frame, which leads to similar results as Extm. Ptb. Sync.

It is also obvious that our method tends to get high accuracy on the preservation ratio of 10%, and adding more pixels to 20% will not contribute to accuracy too much or even will cause lower accuracy (on the R(2+1)D model for EPIC-Object dataset). We suspect that in our experiments, the prediction to the target label for a given video could be mainly decided by the key 10% pixels of the video.